

See discussions, stats, and author profiles for this publication at: <https://www.researchgate.net/publication/272082592>

Nonlinear Chiro-Optical Amplification by Plasmonic Nanolens Arrays Formed via Directed Assembly of Gold Nanoparticles

ARTICLE *in* NANO LETTERS · FEBRUARY 2015

Impact Factor: 13.59 · DOI: 10.1021/nl504613q · Source: PubMed

CITATIONS

5

READS

31

9 AUTHORS, INCLUDING:



[Jeremy White Jarrett](#)

Florida State University

10 PUBLICATIONS 21 CITATIONS

[SEE PROFILE](#)



[Vitaliy Pustovit](#)

52 PUBLICATIONS 288 CITATIONS

[SEE PROFILE](#)



[Kenneth L Knappenberger](#)

Florida State University

63 PUBLICATIONS 548 CITATIONS

[SEE PROFILE](#)

Nonlinear Chiro-Optical Amplification by Plasmonic Nanolens Arrays Formed via Directed Assembly of Gold Nanoparticles

Sushmita Biswas,[†] Xiaoying Liu,[‡] Jeremy W. Jarrett,[§] Dean Brown,[†] Vitaliy Pustovit,[†] Augustine Urbas,[†] Kenneth L. Knappenberger, Jr.,[§] Paul F. Nealey,[‡] and Richard A. Vaia*,[†]

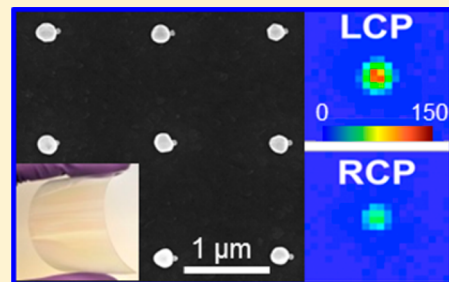
[†]Air Force Research Laboratory, 2941 Hobson Way, Wright Patterson Air Force Base, Ohio 45433, United States

[‡]The Institute for Molecular Engineering, University of Chicago, Chicago, Illinois 60637, United States

[§]Department of Chemistry and Biochemistry, Florida State University, Tallahassee, Florida 32306, United States

Supporting Information

ABSTRACT: Metal nanoparticle assemblies are promising materials for nanophotonic applications due to novel linear and nonlinear optical properties arising from their plasmon modes. However, scalable fabrication approaches that provide both precision nano- and macroarchitectures, and performance commensurate with design and model predictions, have been limiting. Herein, we demonstrate controlled and efficient nanofocusing of the fundamental and second harmonic frequencies of incident linearly and circularly polarized light using reduced symmetry gold nanoparticle dimers formed by surface-directed assembly of colloidal nanoparticles. Large ordered arrays (>100) of these C_{cov} heterodimers (ratio of radii $R_1/R_2 = 150 \text{ nm}/50 \text{ nm} = 3$; gap distance $l = 1 \pm 0.5 \text{ nm}$) exhibit second harmonic generation and structure-dependent chiro-optic activity with the circular dichroism ratio of individual heterodimers varying less than 20% across the array, demonstrating precision and uniformity at a large scale. These nonlinear optical properties were mediated by interparticle plasmon coupling. Additionally, the versatility of the fabrication is demonstrated on a variety of substrates including flexible polymers. Numerical simulations guide architecture design as well as validating the experimental results, thus confirming the ability to optimize second harmonic yield and induce chiro-optical responses for compact sensors, optical modulators, and tunable light sources by rational design and fabrication of the nanostructures.



KEYWORDS: *Directed assembly, gold heterodimers, nanolens, second harmonic generation, circular dichroism*

Owing to the large electromagnetic field enhancements and extinction cross sections of localized surface plasmons, metal nanoparticles (MNPs) and their assemblies have been of interest for a broad range of applications including sensing,^{1–3} photovoltaics,⁴ photodetection,⁵ spectroscopy,^{6,7} and optical information processing.^{8,9} In particular, symmetry-broken systems of MNPs have attracted significant attention due to reported Fano resonances,^{10,11} nanofocusing of electromagnetic fields,^{12,13} and chiro-optical activity.^{14–18} Whereas Fano resonances are of interest for sensing and optical modulators, nanofocusing creates strong local electromagnetic fields, resulting in large amplification of surface-enhanced spectroscopic signals. In addition, these strong local fields generate enhanced nonlinear optical signals, resulting in spatially localized second harmonic generation (SHG)^{18–23} and four-wave mixing signals.²⁴ In this context, a noncentrosymmetric nanoassembly of two or more MNPs has been proposed to function as an electromagnetic antenna, capable of focusing incident fundamental and harmonic waves to nanometer volumes.^{12,18,25} Moreover, these local fields are sensitive to input polarization.^{12,18,26} Chiro-optical activity of metal nanoparticle dimers can result from interfacial chirality²⁷ or multipole–dipole interference between two electromagnetically

coupled nanospheres.^{28–32} As a result, significant interest is evolving to develop artificial chiral materials, materials lacking inversion symmetry that interact differently with specific polarization states of light. Such MNP-based materials would have applications as negative index media, biosensors, and photochemical catalysts. However, the rational design and fabrication of nanoparticle assemblies with predictive, high performance has remained a significant challenge due to the required uniformity and precision of the assembled structure as well as the nanounits. To minimize loss, the latter requires single crystallinity, which is not achievable with current top-down lithography approaches.

Several methods for assembling colloidal MNPs into asymmetric and chiral clusters based on DNA origami,³³ laser ablation,³⁴ and molecular-induced aggregation³⁵ have been developed. However, these techniques are generally not scalable, and the inherent structural heterogeneity across the ensemble of clusters hampers the reproducibility of the optical and electronic properties of these materials. For example,

Received: December 1, 2014

Revised: February 1, 2015

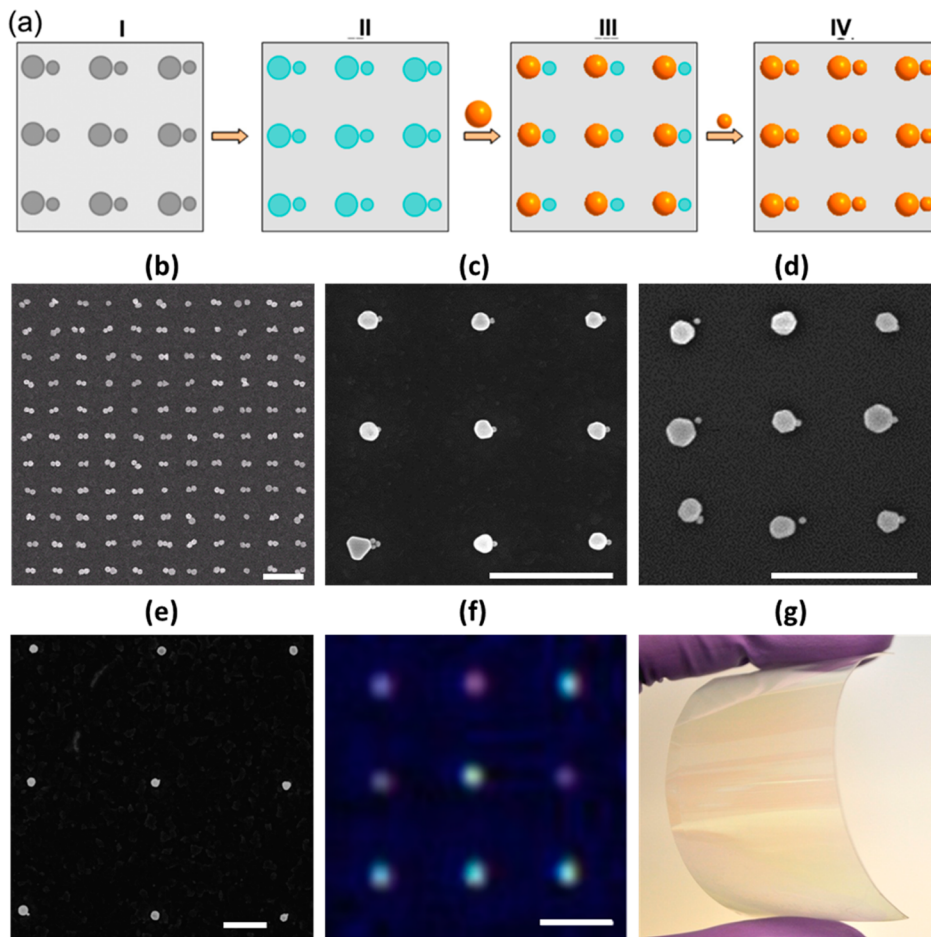


Figure 1. Dimer nanoparticle arrays. (a) Schematic of the process for positioning and patterning of nanoparticles into arrays of hybrid structures on chemically patterned substrates. (I) Creation of nanopatterned surfaces using standard tools of electron beam lithography and oxygen plasma etching; (II) selective surface functionalization by grafting of specific polymer brushes; (III, IV) sequential, site-specific immobilization of nanoparticles for the assembly of nanostructures in large-area arrays. (b–e) SEM images of the arrays of homodimer MNPs (diameters 150 nm) on ITO/glass, heterodimer MNPs (diameters 150 and 50 nm) on ITO-PEN, Si, and ITO/glass substrates, respectively. Scale bars represent 1 μm . (f) Optical scattering image of the array of heterodimers. Scale bar represent 2.5 μm . (g) ITO-PEN after being peeled off from rigid alumina support.

single-particle second harmonic generation–circular dichroism ratio (SHG-CDR) measurements reveal large structure-specific CDR polydispersity over multiple MNP dimers formed by thiol-mediated assembly.^{19,36} These limitations may be overcome by using a surface-directed assembly approach, which combines top-down lithography and bottom-up chemical synthesis, allowing structural precision and reproducibility of the assembled MNPs at large scale.

Herein, we demonstrate the fabrication of novel architectures of symmetric (homo) and asymmetric (hetero) gold nanoparticle dimer arrays using a surface-directed assembly approach³⁷ that simultaneously provides nano-, micro-, and macroarchitectural precision. We provide numerical and experimental verification that these nanostructures support Fano resonances and are capable of focusing the fundamental and second harmonic incident waves to the interparticle gaps of the nanoscale architectures. In addition, asymmetric heterodimers gave rise to circular dichroism in the nonlinear optical signal. The SHG yield of the heterodimer exceeded that of the homodimer by a factor of 2.39 ± 0.55 . On the basis of the dimensions of the heterodimer nanospheres and numerical simulations, the observed circular dichroism is attributed primarily to multipolar–dipolar interference. The versatility of the assembly process was demonstrated on a variety of

substrates (including polymers), paving a novel and robust route to flexible integrated photonics that incorporate these assembled plasmonic nanostructures as compact and low-cost sensors, optical modulators, and tunable light sources in the UV-NIR spectral range.

Arrays of gold MNP dimers were synthesized by a directed assembly approach, Figure 1a, whereby a combination of top-down electron beam lithography and bottom-up chemical synthesis³⁷ was applied on an indium tin oxide ITO/glass substrate (Synthesis details in Supporting Information). Briefly, a clean ITO-glass substrate was spin coated with cross-linkable polystyrene (PS), which served as the imaging layer. The imaging layer was then spin coated with a poly(methyl methacrylate) (PMMA) resist. Electron beam lithography was used to create patterns in various geometries and arrangements. The patterned substrates were then subject to development. These patterns were transferred to the PS layer by exposure to oxygen plasma with a reactive ion etcher. The patterned substrates were functionalized with poly(ethylene glycol) methyl ethers (PEG-OH) by spin coating from solution and annealing. The remaining photoresist was then removed. Gold nanoparticles, stabilized with surface citrate, of different sizes were sequentially adsorbed onto specific regions (pads) based on an affinity prescribed by pattern size and PEG molecular

weight.³⁷ Each nanoparticle solution was spotted on the patterned area for 40 min in a Petri-dish sealed with parafilm and containing 1 mL of water. Au nanoparticles were selectively adsorbed onto the PEG regions by means of hydrogen bonding between the PEG moieties and surface citrate.³⁷ The substrate was then rinsed with water and dried with nitrogen. The adsorption process was repeated with a different size of gold MNPs for sequential immobilization to generate multi-component nanostructures. Of special note, the process of positioning two spheres on top of adjacent pads enables an effective size reduction of the distance between the pads relative to the distance between the spheres' surfaces due to the geometry of a sphere with a larger diameter than the dimension of the pad. This process is applicable over a variety of substrates as shown in Figure 1b–g, ITO-PEN (200 nm ITO on polyethylene naphthalate, Arizona State University, Flexible Electronics and Display Center), silicon, and ITO/glass, respectively, demonstrating the versatility of the process. Linear and nonlinear optical images of the arrays (e.g., dark-field optical image of heterodimer array on ITO-glass, Figure 1f) only show optical effects at the intended array nodes, and not between nodes or randomly scattered across the substrate. All optical measurements, as discussed below, were conducted with samples fabricated on ITO-glass substrates. Taken together, the SEM and optical images shown in Figure 1 reflect long-range order of the plasmonic nanostructures.

In order to examine the nanoscale structural uniformity of the plasmonic arrays, single particle SHG images were compared to the optical and electron microscope images. Representative SEM images of homo- and heterodimers are shown in Figure 2a,b. In this example, the homodimer consists of two gold MNPs with diameters of 150 nm separated by a gap distance of 1–10 nm with 85% yield based on electron microscopy. The heterodimer sample, composed of gold MNPs having diameters of 150 and 50 nm and an interparticle gap of 1–10 nm, shows a yield in excess of 25% by electron microscopy. Polarization-dependent SHG images were acquired to quantitatively analyze the nanoparticle alignment precision for the fabrication method. The structural control revealed in the SEM and optical scattering images of nanoparticle arrays in Figure 1 is also apparent in the polarization-resolved SHG image in Figure 2c. Images acquired when the polarization plane of the fundamental wave is oriented parallel (Figure 2c; top) or perpendicular (Figure 2c; bottom) with respect to the dimer-interparticle axis show uniform bright and dark responses, respectively, from the nodes of the assembled homodimer array. The paucity of signal for the perpendicular polarization of the SHG signal occurs because this orientation excited a “dark” plasmon mode.³⁸ In concert, the maximum SHG signal from the homodimers also occurs when the incidence angle of plane-polarized fundamental light is oriented parallel to the interparticle axis; reflecting a dipolar response (Supporting Information Figure S4) and the revealing the dimer interparticle (i.e., major) axis. On the basis of this polarization-dependent approach, the orientations of 92 individual homodimer nanostructures (Figure 2d) in the array were determined, and the results are displayed in Figure 2d as a histogram. The data revealed that the orientation of the major axes for approximately 50% of the measured individual homodimer nanostructures were within an acceptance angle of $\pm 10^\circ$. The major axes of ~95% of the particles were aligned within an acceptance angle of $\pm 35^\circ$. A movie portraying the polarization-dependent SHG response from an array of

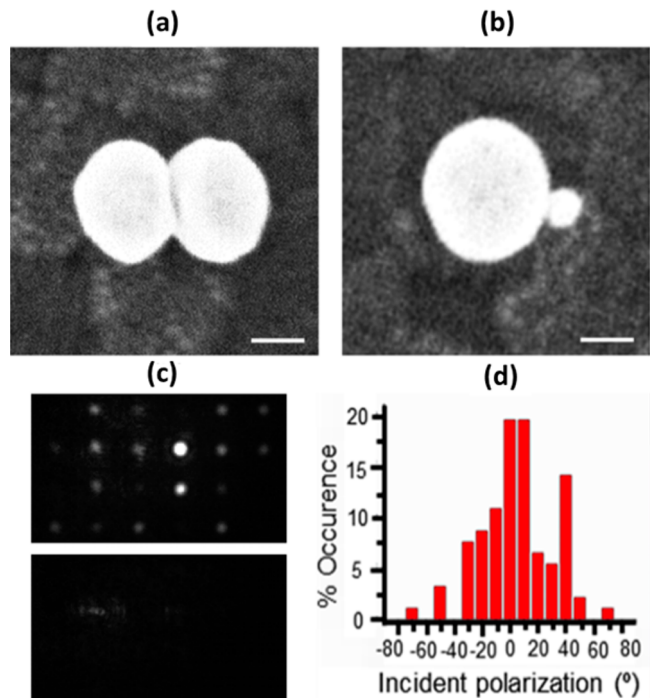


Figure 2. Local dimer structure. (a,b) SEM images of individual homodimer and heterodimer structures. Scale bars represent 75 nm. (c) Polarization-resolved second harmonic generation (SHG) image with incident polarization parallel and perpendicular to the interparticle axis showing uniform bright and dark response from an array of assembled homodimers. (movie provided in Supporting Information). (d) Histogram depicting the percentage of homodimers with interparticle axis aligned along the horizontal incident polarization. Data was obtained by measuring the SHG signal as a function of incident polarization angle and recording when the maximum SHG signal occurred for each particle. 0° was defined as the angle where the highest percentage of particles had a maximum SHG signal.

homodimer nanoparticles is included in Supporting Information (Supporting Video 1). On the basis of these nonlinear optical data, structural control in the fabrication process clearly enabled production of photonic nanomaterials with uniform optical properties at the nanoscale. Further results on synthesis optimization in order to achieve higher yields will be published in a forthcoming study. The 3:1 ratio of the diameters of the NPs comprising the heterodimer was chosen according to the proposed plasmonic nanolens geometry^{12,18} in order to achieve nanometer focusing of the linear and second harmonic (SH) optical fields. The results presented in Figures 1 and 2 demonstrate the capacity for precise positioning of Au MNPs of both equivalent and different diameters at large scale while maintaining a uniform nanoscale optical response, indicating that this surface-directed assembly holds great promise for integration of nanoplasmonic structures in nanophotonics.

The optical characterization of a representative homodimer (diameter 150 ± 2 nm; gap 1 ± 0.5 nm; symmetry point group $D_{\infty h}$) in the array is summarized in Figure 3. Single-particle scattering spectra (Figure 3a) with linearly polarized excitation oriented either parallel (black) or perpendicular (red) to the interparticle axis were collected using an Olympus BX41 optical dark-field scattering microscope coupled to a spectrometer and a charge-coupled device (CCD) camera. Spectra were correlated with SEM images to determine the structural

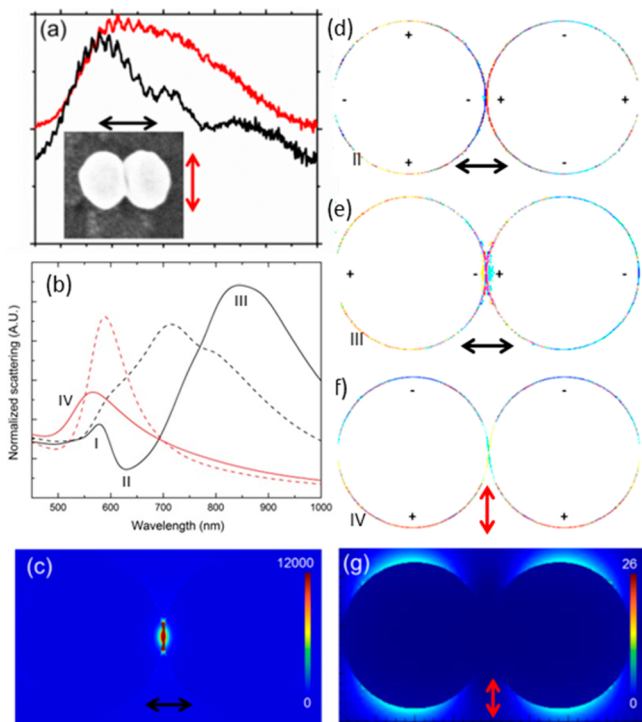


Figure 3. Homodimer. (a) Experimental dark-field scattering spectra for parallel (black curve, black arrow) and perpendicular (red curve, red arrow) polarizations from a homodimer comprised of 150 nm diameter nanoparticles shown in the SEM image in the inset. (b) Modeled scattering spectra for parallel (black curve) and perpendicular (red curve) polarizations from a homodimer of nanoparticles of diameter 150 nm separated by a gap of 1 nm (solid line) and 7.5 nm (dashed line) gap on glass. For the 1 nm gap, (c,g) electric-field enhancements for parallel and perpendicular polarizations, as well as (d,e) mode profiles for parallel polarization at the dip at II and the lower energy peak III, respectively; and (f) for perpendicular polarization at peak IV. +,− symbols included to convey average charge distribution.

parameters of the nanostructures.³⁹ The scattering spectra is very sensitive to interparticle spacing, as indicated in Figure 3b by comparing the calculated scattering spectrum for ideal homodimers with 1 (solid) and 7.5 nm (dashed) gaps on glass (Lumerical Solutions v8, FDTD modeling details provided in Supporting Information S.IV).^{10,40} In general, the experimental spectra from single homodimers qualitatively agree with calculated scattering from ideal homodimers with an interparticle gap in the range of 1–4 nm. As the interparticle spacing decreases, scattering from excitation polarized perpendicular (red) to the interparticle is similar. However, for excitation polarized parallel (black) to the interparticle axis, the scattering splits into two peaks at 560 nm (I) and 850 nm (III) separated by a shallow dip at 630 nm (II). These are characteristic of a Fano resonance. The higher-energy peak and the dip correspond to the quadrupolar charges in the individual MNPs (Figure 3d). The lower-energy peak (III) corresponds to the dipolar-bonding mode in the MNPs as shown in Figure 3e. In contrast, for polarization perpendicular to the interparticle axis (red arrow, red curve), a single peak at 560 nm (IV) is observed, which corresponds to the dipolar antibonding mode in the dimer, as shown in Figure 3f. Figure 3c,g shows the calculated electric field enhancement with the excitation source polarized parallel and perpendicular to the interparticle axis, respectively. When the polarization is parallel

to the axis, a strong field enhancement and confinement to the interparticle gap is predicted based on the numerical results. When the polarization is oriented perpendicular to the dimer axis, the confinement is not present, and the enhancement decreases. As the interparticle spatial separation between the two particles is increased, the magnitude of the E-field enhancement decreases, and the higher-order interacting modes disappear (Supporting Information Figure S5). Overall, the numerical analyses and experimental scattering spectra of the homodimer system demonstrate the variation of the field enhancement with polarization and gap distance, as well as Fano interference effects, both of which are characteristic of plasmonic nanolenses.^{12,41}

The impact of reducing dimer symmetry on the field confinement and plasmonic interference is shown in Figure 4

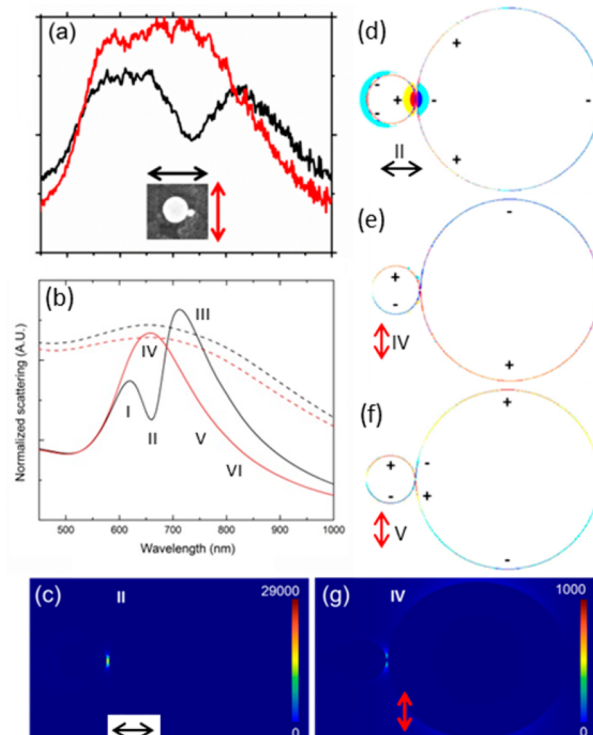


Figure 4. Heterodimer. (a) Experimental dark-field scattering spectra for parallel (black curve, black arrow) and perpendicular (red curve, red arrow) polarizations from a heterodimer comprised of 150 and 50 nm diameter nanoparticles as shown in the SEM image in the inset. (b) Modeled scattering spectra for parallel (black curve) and perpendicular (red curve) polarizations from a heterodimer of nanoparticles of diameter 150 and 50 nm separated by 1 nm (solid lines) and 7.5 nm (dashed lines) on glass. For 1 nm separation, (c,g) electric field enhancements for parallel and perpendicular polarizations. Associated mode profiles at 1 nm separation for parallel polarization at (d) dip II and for perpendicular polarization at (e) peak IV and a lower energy at (f) V (680 nm). +,− symbols included to convey average charge distribution.

via the optical response and the associated mode profile of a representative gold MNP heterodimer in the array. This heterodimer was comprised of two gold MNPs separated by a gap of 1.0 ± 0.5 nm (left MNP, $D_l = 150 \pm 2$ nm; right MNP, $D_r = 50 \pm 2$ nm). An SEM image of the heterodimer structure is displayed in the inset in Figure 4a. Compared to the homodimer structure, the heterodimer structure lacks inversion symmetry and thus belongs to the lower-symmetry C_{ov} point

group. The experimental scattering spectrum generated using an excitation source that is polarized parallel to the interparticle axis (Figure 4a) shows a pronounced dip at ~ 700 nm (II), characteristic of a Fano resonance. This spectral response is reproducible across numerous clusters with similar asymmetric structure (Supporting Information Figure S2). The Fano interference from the heterodimer is much more pronounced than that measured for the homodimer.⁴¹ This is also conveyed in the calculated scattering spectra (Figure 4b) of ideal heterodimers (150 and 50 nm) with 1 (solid) and 7.5 nm (dashed) gaps on glass. In general, the experimental spectra from single heterodimers qualitatively agree with calculated scattering from ideal heterodimers with an interparticle gap in the range of 1–4 nm. For example, the modeled spectra at 1 nm (Figure 4b) reproduces the experimental features with a spectral shift of ~ 100 nm that may be attributed to the uncertainties in determining the exact shape, size, surface roughness, and gap distance.^{9,10} The pronounced dip and the higher-energy peak corresponds to higher-order quadrupole–quadrupole coupling mixed with dipole modes in the heterodimer (Figure 4d and Supporting Information Figure S6.c), which indicated the heterodimer should exhibit chiro-optical activity. The lower-energy peak corresponds to the dipole–dipole bonding mode (Supporting Information Figure S6.b). For linear polarization oriented perpendicular to the interparticle gap, a superposition of modes appears at different wavelengths, although not as resonance peaks (Figure 4e,f and Supporting Information Figure S6.d). For example, the peak at 600 nm (IV) consists of a dipole–dipole antibonding mode; the spectral contribution at 680 nm (V) consists of a dipole mode in the smaller MNP and dipole and quadrupole modes in the larger MNP; and the spectral region at 716 nm consists of dipole–dipole bonding modes (Supporting Information Figure S6.d). Figure 4c,g confirms that the incident electromagnetic fields are confined in the interparticle gap for plasmon excitation polarized parallel to the dimer axis, while these effects are significantly smaller for the perpendicular polarization. Compared to the symmetric homodimer, the numerically simulated electric field enhancements are about a factor of 2.3 higher for the asymmetric nanolens heterodimer. As the distance between the two spheres is increased from 1.0 to 7.5 nm in the simulations, the Fano profile disappears (Figure 4b) and the strongest field enhancement occurs at a wavelength of 960 nm, which is red-shifted from the plasmon resonance at 620 nm as depicted in Supporting Information Figure S7. Thus, the asymmetric MNP dimers act as a nanolens leading to off-resonant focusing of the electromagnetic fields, which is similar to the theoretically predicted behavior of larger, trimeric nanolenses.¹²

In addition to the enhancement of the linear optical fields, the asymmetric heterodimer nanostructures also exhibit enhanced nonlinear optical second harmonic generation (SHG) (Figure 5). The numerically simulated spectra shown in Figure 5a indicate a strong second harmonic component for a prototypical heterodimer (diameters 150 and 50 nm with a gap distance of 1 nm) with contributions from both electric and magnetic dipoles. Note that the size-dependent absolute average second-order nonlinear polarizabilities of gold MNPs have been incorporated into the model ($\chi_{150} = 1.68 \times 10^{-13}$, $\chi_{50} = 3.94 \times 10^{-13} \text{ m/V}$).⁴² The accompanying numerically generated SH field localization maps for polarization parallel to the homo- and heterodimer interparticle axis (Figure 5c,d) shows that the SH fields are confined between the MNPs; and

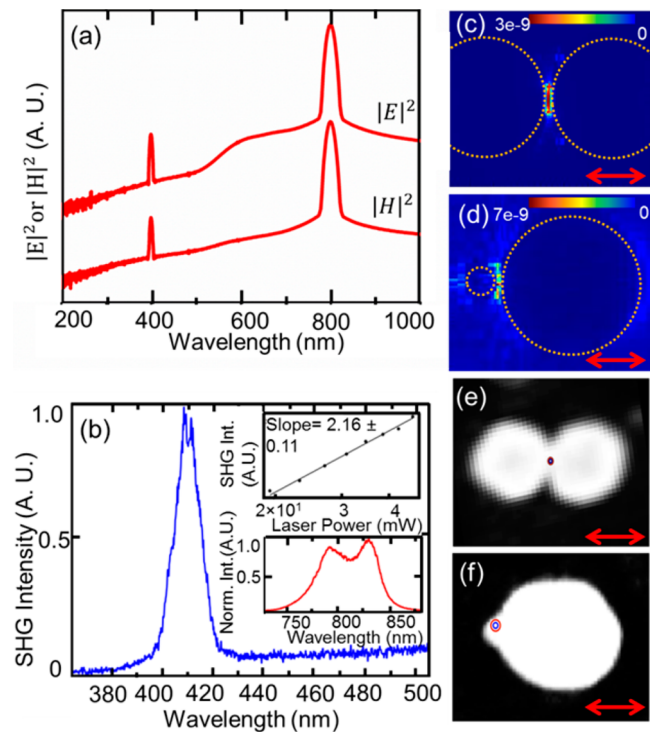


Figure 5. SHG field localization. (a) Modeled SHG signal from a heterodimer (diameters 150 and 50 nm with a gap distance of 1 nm). (b) Experimental SHG signal from a heterodimer. A discrete peak at the second harmonic wavelength (410 nm) is observed. Inset shows integrated SH intensity as a function of incident laser power plot on a log–log axis. A quadratic power dependence (solid curve) confirms that the signal results from a second-order nonlinear optical process. (c,d) Modeled SHG field intensity maps depicting the location of hot spots in a homodimer (diameters 150 nm, 150 nm, and gap 1 nm) and heterodimer, respectively. Dashed circles denote the nanoparticle surface. (e,f) Experimental SH field localization maps from a homodimer and heterodimer respectively in agreement with model.

there is a factor of 2.33 times stronger enhancement in the heterodimer compared to the homodimer.

In order to test the numerical predictions, the relative SHG yield and positions of the SH source were determined for the homo- and heterodimers. The SHG signal was recorded by a custom-built transmission nonlinear optical microscope coupled to a mode-locked Ti-sapphire laser excitation source (80 MHz, Coherent Mantis) with a fundamental input pulse width of 65 fs and a center wavelength of 810 nm (the experimental setup is depicted in Supporting Information Figure S3). A linear polarizer was placed in the beam path to ensure high extinction ratio of the linearly polarized source. The laser was focused to the sample using an aspherical lens. SH photons were collected with a 100 \times (1.25 numerical aperture) oil-immersion microscope objective, isolated from the fundamental using a series of optical filters (short-pass, Chroma Technology, 680 nm; band-pass, Chroma technology, HQ 400/20m-2P, centered at 400 nm), and focused to the entrance slit of a spectrometer (Andor Technology, Shamrock 303i) that was coupled to a cooled electron multiplying charge-coupled device (Andor Technology, iXon Ultra 897). For SHG localization measurements, the light passed through a half-wave plate before the focusing lens in order to rotate the plane of polarization parallel to the nanostructure principle axis. The nonlinear optical localization procedure has been described

previously.^{19,26} Essential details are provided in the Supporting Information. Figure 5b provides an example SHG spectrum from a heterodimer. In both homo- and hetero- structures, SH hot spots were experimentally observed to be localized in the gaps between the MNPs as shown in Figure 5e and f. Two concentric rings representing 1- and 2- σ confidence intervals indicated the determined hotspot position. The procedure for this localization analysis and overlay is described in the Supporting Information. SHG yield was determined for both asymmetric and symmetric MNP dimers by calculating the ratio of the number of detected harmonic photons per incident fundamental photon. Based on this analysis, we determined that the SHG yield of the heterodimer is 2.39 ± 0.55 times greater than that noted for the homodimer, which is in excellent agreement with the simulated enhancement factor of 2.3, as shown in Figure 5c,d. Thus, the simulated SHG spectrum (Figure 5a) and field localization intensity maps (Figure 5c,d) provide excellent agreement with the experiments (Figure 5e,f). These two experimental observations, which were consistent over a large sample set, are in good agreement with the theoretical model for the photonic nanolens.

Next, the impact of structure geometry on the chiro-optic SHG response was analyzed with SHG-CDR measurements. For the SHG-CDR measurements, a quarter-wave plate was inserted before the focusing lens to generate left and right circularly polarized (LCP and RCP) light at the sample plane. As expected based on simulated plasmon-mode structure and presence of coupled multipole–dipole modes, the second order responses from the low-symmetry heterodimer nanostructures exhibit chiro-optical behavior, as confirmed by nonzero CDR observed in the SHG field maps for LCP and RCP excitation (Figure 6). The CDR was obtained for individual nanostruc-

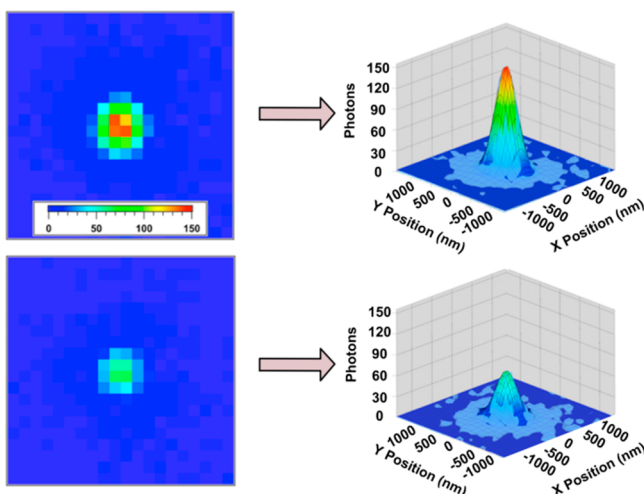


Figure 6. Circular dichroism in heterodimers. SHG field map localization for LCP (top) and RCP (bottom) light obtained from a gold nanoparticle heterodimer. The corresponding raw 3D SHG data with an overlay of 2D Gaussian fits are depicted on the right.

tures by exciting them using left and right circularly polarized states of incident fundamental light and measuring the resultant SH intensity. We note that depolarization analysis of the SH signal yields a dipolar pattern when linearly polarized fundamental light is aligned along the interparticle axis (Supporting Information Figure S4). SHG-CDR is computed by²⁶

$$\text{SHG-CDR} = \left| \frac{2(I_{2\omega}^{\text{LCP}} - I_{2\omega}^{\text{RCP}})}{I_{2\omega}^{\text{LCP}} + I_{2\omega}^{\text{RCP}}} \right|$$

where $I_{2\omega}$ is the intensity of the experimentally measured SHG signal for the LCP and RCP excitation. The raw SH data are overlaid with the corresponding 2D Gaussian fit (Figure 6 right). In this case, the measured SH intensity differs by a factor of approximately 2 between LCP and RCP excitation demonstrating the chiro-optical response of the heterodimer nanolens geometry. The corresponding SHG-CDR for this nanostructure was measured to be 0.76 ± 0.07 similar to reported SHG-CDR values for chiral nanostructures.²⁶ The average differential response from a survey of over 10 heterodimer structures varies less than 20%, reflecting the quality and reproducibility of the surface directed assembly in lieu of the strong sensitivity of the CDR to structural variation. This is in stark contrast to prior studies.^{26,36,43} For example, SHG-CDR values obtained for solid gold nanosphere dimers formed by thiol-mediated aggregation varied widely (160% between 0.39 and 1.83 around the average value),⁴³ precluding assignment of an ensemble-averaged values. The comparatively narrow distribution of SHG-CDR values reported here reflects the superior capacity of the directed assembly process for fabricating nanophotonic arrays with predictive optical properties over alternative approaches. Note that the homodimers also display CDR, albeit a low average value of 0.16 ± 0.06 . We attribute this response to the presence of small interfacial heterogeneities at the interparticle interface from the inherent structural heterogeneity of the gold nanoparticle building blocks. Multipolar modes could also contribute to the nonzero CDR of the homodimer, but our numerical simulations suggest the response is predominantly dipolar in nature at the fundamental wavelength. Overall, the statistical trend across the homo- and heterodimer arrays unambiguously demonstrates strong circular dichroism in heterodimers compared to homodimers. We attribute multipole-dipole interference as the primary source of the CDR in the heterodimers based on the numerical simulations of coupled modes between the large and small nanoparticles. Thus, the asymmetric nanolens dimers are highly efficient in focusing electromagnetic energy at fundamental and harmonic wavelengths to nanoscale volumes and capable of supporting chiral optical response based on plasmonic modes at optical frequencies. Moreover, the fabrication approach used here generates nanostructures with predictive structure-dependent optical properties.

In conclusion, we report efficient nanofocusing of linear and second harmonic optical signals across large arrays of rationally designed asymmetric gold nanoparticle dimers. Both symmetric and asymmetric nanoparticle dimers were studied using numerical and experimental single-particle optical methods, providing unambiguous validation that two-component metal nanoparticle assemblies formed by directed assembly can function as efficient nanolenses. In addition, we demonstrate that the directed assembly method can be used to fabricate nanostructures with predictive nonlinear and chiro-optical properties. In regard to reproducibility and prospects for scale-up, these methods are more promising than other nanoparticle assembly techniques. Therefore, the surface-directed assembly approach provides a novel platform that can be used for rational development of numerous nanophotonic materials, which can be extended to form nanostructures composed of multiple nanoparticles with high

spatial precision. Furthermore, the versatility of the assembly process was demonstrated on a variety of substrates. The suite of nanostructures generated by this directed assembly technique holds immense potential for photonic applications including negative index materials, biosensors, and catalysis.

■ ASSOCIATED CONTENT

Supporting Information

Further information on the synthesis, modeling, and characterization of the heterodimers. This material is available free of charge via the Internet at <http://pubs.acs.org>.

■ AUTHOR INFORMATION

Corresponding Author

*E-mail: Richard.Vaia@us.af.mil. Phone: 937-785-9209. Fax: 937-656-6327.

Notes

The authors declare no competing financial interest.

■ ACKNOWLEDGMENTS

Portions of this research are based on work supported by the U.S. Air Force Office of Scientific Research under AFOSR awards FA9550-10-1-0300 and FA8650-090-D-5037. K.L.K acknowledges support from a National Science Foundation (NSF) award, Grant CHE-1150249. Special appreciation is extended to Mark Strnad at ASU Flexible Electronics and Display Center (U.S. Army RDECOM) for supplying the ITO-PEN substrate.

■ REFERENCES

- (1) Wu, C.; Khanikaev, A. B.; Adato, R.; Arju, N.; Yanik, A. A.; Altug, H.; Shvets, G. *Nat. Mater.* **2012**, *11*, 69–75.
- (2) Hao, F.; Sonnenaud, Y.; Dorpe, P. V.; Maier, S. A.; Halas, N. J.; Nordlander, P. *Nano Lett.* **2008**, *8*, 3983–3988.
- (3) Liu, N.; Pucci, A. *Nat. Mater.* **2012**, *11*, 9–10.
- (4) Pillai, S.; Green, M. A. *Sol. Energy Mater. Sol. Cells* **2010**, *94*, 1481–1486.
- (5) Fan, P.; Chettiar, U. K.; Cao, L.; Afshinmanesh, F.; Engheta, N.; Brongersma, M. L. *Nat. Photonics* **2012**, *6*, 380–385.
- (6) Xu, H.; Aizpurua, J.; Kall, M.; Apell, P. *Phys. Rev. E* **2000**, *62*, 4318–4324.
- (7) Wang, J.; Yang, L.; Boriskina, S.; Yan, B.; Reinhard, B. M. *Anal. Chem.* **2011**, *83*, 2243–2249.
- (8) Beausoleil, R. G.; Munro, W. J.; Rodrigues, D. A.; Spiller, T. P. *J. Mod. Optics* **2004**, *51*, 2441–2448.
- (9) Biswas, S.; Duan, J.; Nepal, D.; Park, K.; Pachter, R.; Vaia, R. A. *Nano Lett.* **2013**, *13*, 6287–6291.
- (10) Biswas, S.; Duan, J.; Nepal, D.; Pachter, R.; Vaia, R. *Nano Lett.* **2013**, *13*, 2220–2225.
- (11) Luk'yanchuk, B.; Zheludev, N. I.; Maier, S. A.; Halas, N. J.; Nordlander, P.; Giessen, H.; Chong, C. T. *Nat. Mater.* **2010**, *9*, 707–715.
- (12) Li, K.; Stockman, M. I.; Bergman, D. J. *Phys. Rev. Lett.* **2003**, *91*, 227402.
- (13) Gramotnev, D. K.; Bozhevolnyi, S. I. *Nat. Photonics* **2014**, *8*, 13–22.
- (14) Fan, Z.; Zhang, H.; Govorov, A. O. *J. Phys. Chem. C* **2013**, *117*, 14770–14777.
- (15) Yan, W.; Ma, W.; Kuang, H.; Liu, L.; Wang, L.; Xu, L.; Xu, C. J. *Phys. Chem. C* **2013**, *117*, 17757–17765.
- (16) Frank, B.; Yin, X.; Schaferling, M.; Zhao, J.; Hein, S. M.; Braun, P. V.; Giessen, H. *ACS Nano* **2013**, *7*, 6321–6329.
- (17) Canfield, B. K.; Kujala, S.; Jefimovs, K.; Turunen, J.; Kauranen, M. *Opt. Express* **2004**, *12*, 5418–5423.
- (18) Li, K.; Stockman, M. I.; Bergman, D. J. *Phys. Rev. B* **2005**, *72*, 153401.
- (19) Jarrett, J. W.; Chandra, M.; Knappenberger, K. L. *J. Chem. Phys.* **2013**, *138*, 1–8.
- (20) Slablab, A.; Le Xuan, L.; Zielinski, M.; de Wilde, Y.; Jacques, V.; Chauvat, D.; Roch, J.-F. *Opt. Express* **2012**, *20*, 220–227.
- (21) Canfield, B. K.; Husu, H.; Laukkanen, J.; Bai, B.; Kuittinen, M.; Turunen, J.; Kauranen, M. *Nano Lett.* **2007**, *7*, 1251–1255.
- (22) Butet, J.; Duboisset, J.; Bachelier, G.; Russier-Antoine, I.; Benichou, E.; Jonin, C.; Brevet, P.-F. *Nano Lett.* **2010**, *10*, 1717–1721.
- (23) Kauranen, M.; Zayats, A. V. *Nat. Photonics* **2012**, *6*, 737–748.
- (24) Masia, F.; Langbein, W.; Watson, P.; Borri, P. *Opt. Lett.* **2009**, *34*, 1816–1818.
- (25) Stockman, M. I.; Bergman, D. J.; Anceau, C.; Brasselet, S.; Zyss, J. *Phys. Rev. Lett.* **2004**, *92*, 057402–1–4.
- (26) Jarrett, J. W.; Herbert, P. J.; Dhuey, S.; Schwartzberg, A. M.; Knappenberger, K. L. *J. Phys. Chem. A* **2014**, *118*, 8393–8401.
- (27) Wu, X. L.; Xu, L. G.; Liu, L. Q.; Ma, W.; Yin, H. H.; Kuang, H.; Wang, L. B.; Xu, C. L.; Kotov, N. A. *J. Am. Chem. Soc.* **2013**, *135*, 18629–18636.
- (28) Kauranen, M.; Verbiest, T.; Maki, J. J.; Persoons, A. *J. Chem. Phys.* **1994**, *101*, 8193–8199.
- (29) Kauranen, M.; Verbiest, T.; Persoons, A. *J. Mod. Opt.* **1998**, *45*, 403–423.
- (30) Naguleswaran, S.; Reid, M. F.; Stedman, G. E. *Chem. Phys.* **2000**, *256*, 207–212.
- (31) Barron, L. D.; Buckingham, A. D. *Chem. Phys. Lett.* **2010**, *492*, 199–213.
- (32) Tian, X. R.; Fang, Y. R.; Zhang, B. L. *ACS Photonics* **2014**, *1*, 1156–1164.
- (33) Ding, B.; Deng, Z.; Yan, H.; Cabrini, S.; Zuckermann, R. N.; Bokor, J. *J. Am. Chem. Soc.* **2010**, *132*, 3248–3249.
- (34) Kneipp, J.; Li, X.; Sherwood, M.; Panne, U.; Kneipp, H.; Stockman, M. I.; Kneipp, K. *Anal. Chem.* **2008**, *80*, 4247–4251.
- (35) Bidault, S.; Polman, A. *Int. J. Opt.* **2012**, *2012*, 1–5.
- (36) Chandra, M.; Dowgiallo, A.-M.; Knappenberger, K. L. *J. Am. Chem. Soc.* **2012**, *134*, 4477–4480.
- (37) Onses, M. S.; Nealey, P. F. *Small* **2013**, *9*, 4168–4174.
- (38) Jarrett, J. W.; Chandra, M.; Knappenberger, K. L., Jr. *J. Chem. Phys.* **2013**, *138*, 214202.
- (39) Biswas, S.; Nepal, D.; Park, K.; Vaia, R. A. *J. Phys. Chem. Lett.* **2012**, *3*, 2568–2574.
- (40) Pustovit, V.; Biswas, S.; Vaia, R.; Urbas, A. *J. Opt.* **2014**, *16*, 114010.
- (41) Brown, L. V.; Sobhani, H.; Lassiter, J. B.; Nordlander, P.; Halas, N. J. *ACS Nano* **2010**, *4*, 819–832.
- (42) Griffin, J.; Singh, A. K.; Senapati, D.; Lee, E.; Gaylor, K.; Jones-Boone, J.; Ray, P. C. *Small* **2009**, *5*, 839–845.
- (43) Chandra, M.; Knappenberger, K. L. *Phys. Chem. Chem. Phys.* **2013**, *15*, 4177–4182.